High-pressure developments for resonant X-ray scattering experiments at I16

I. Povedano,[a,b]* A. Bombardi,[b,c] D. G. Porter,[b] M. Burt,[b] S. Green[b] and K. V. Kamenev[a]

[a]School of Engineering and Centre for Science at Extreme Conditions, The University of Edinburgh, Edinburgh EH9 3FD, UK, [b]Diamond Light Source Ltd, Harwell Science and Innovation Campus, Didcot OX11 3PU, UK, and [c]Clarendon Laboratory, Department of Physics, University of Oxford, Parks Road, Oxford OX1 3PU, UK. *Correspondence e-mail: isabel.povedano@diamond.ac.uk

An experimental setup to perform high-pressure resonant X-ray scattering (RXS) experiments at low temperature on I16 at Diamond Light Source is presented. The setup consists of a membrane-driven diamond anvil cell, a panoramic dome and an optical system that allows pressure to be measured *in situ* using the ruby fluorescence method. The membrane cell, inspired by the Merrill–Bassett design, presents an asymmetric layout in order to operate in a back-scattering geometry, with a panoramic aperture of $100°$ in the top and a bottom half dedicated to the regulation and measurement of pressure. It is specially designed to be mounted on the cold finger of a 4 K closed-cycle cryostat and actuated at low-temperature by pumping helium into the gas membrane. The main parts of the body are machined from a CuBe alloy (BERYLCO 25) and, when assembled, it presents an approximate height of 20–21 mm and fits into a 57 mm diameter. This system allows different materials to be probed using RXS in a range of temperatures between 30 and 300 K and has been tested up to 20 GPa using anvils with a culet diameter of 500 μm under quasi-cryogenic conditions. Detailed descriptions of different parts of the setup, operation and the developed methodology are provided here, along with some preliminary experimental results.

1. Introduction

A plethora of phenomena such as multiferroicity (Lee *et al.*, 2013), metal–insulator transitions (Calder *et al.*, 2012), charge-ordering (Pascut *et al.*, 2011), solving the magnetic structure of frustrated magnets (Agrestini *et al.*, 2008; Biffin *et al.*, 2014) or the distribution of magnetic domains (Fabrizi *et al.*, 2010; Waterfield-Price *et al.*, 2016) have been understood using the resonant X-ray scattering (RXS) technique. The RXS technique is based on the enhancement of the magnetic scattering cross-section that occurs when the energy of the incoming beam is tuned to the proximity of an absorption edge of the magnetic element of interest (Gibbs *et al.*, 1988; Hill & McMorrow, 1996). During the resonant process, electrons from a specific electronic level in the core are promoted to a virtual state near the Fermi level and immediately decay (Blume & Gibbs, 1988), emitting a photon with the same energy as the incident one. This powerful combination of spectroscopic information via the access to the specific projection of the electronic density of states and crystallographic capability via the sensitivity to periodic arrangements of electrons and magnetic moments in crystalline materials provides a unique source of information that has proven invaluable in understanding many complex electronic phenomena.

351
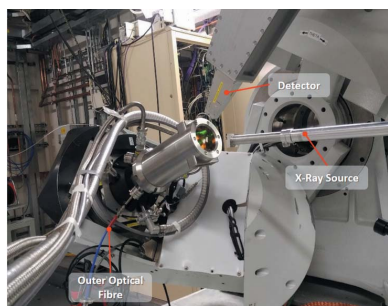
All the electronic arrangements mentioned above are particularly sensitive to the spatial distribution of the atoms involved in the correlation. By applying pressure we can induce changes in the crystal lattice, varying the orbital overlapping – distance and angle between atomic orbitals – and therefore we may affect directly the relative strength and in some cases the relative sign of the magnetic exchange interactions. Thus, using pressure, new exciting ground states can become accessible, such as for the case of the recently achieved high-temperature superconductivity on LaH_{10} (Drozdov *et al.*, 2019), the pressure-induced ferroelectricity in $GdMn_2O5$ (Poudel *et al.*, 2015) or the tuning of the metal–insulator transition in Ca_2RuO_4 (Nakamura, 2007).

Historically, the device most commonly used for high-pressure (HP) experiments due to its compact design and large range of pressures reachable is the diamond anvil cell (DAC). In a DAC, the sample, a single crystal in RXS experiments, is placed between the flat tips of two opposed diamond anvils and confined in the hole of a metallic gasket. In this chamber, pressure is generated by applying force on the anvils (see Fig. 1). In order to generate isotropic pressure, the sample space is also filled with a pressure-transmitting media (PTM) (gas, liquid or solid) which helps to maintain hydrostatic conditions. Additionally, we place a pressure marker in the sample chamber – a substance with a well known response to applied pressure such as an *in situ* pressure gauge.

Despite the potential of the combination of HP and RXS, there are not many examples in the literature using these two techniques, mainly due to the technical difficulties associated with the experimental setup, discussed in the next section, and the fact that the enhancement of the resonant signal is large only for dipolar transitions from electrons in the core towards semi-occupied electronic levels responsible for the magnetic properties of the material, in the presence of a strong spin–orbit coupling. Only under these conditions is the enhancement of the resonant signal large, facilitating the detection of the scattered signal. Most of these phenomena require low temperature to stabilize the electron-correlated state, which makes the manipulation of a DAC more complex due to the need of mechanisms for remote actuation. Additionally, the increase of the dissipation in the transmitted force due to the increased friction at low temperature, the limited space

available inside the cryogenic equipment and the possible variations in the thermal contractions of the different parts of the cell represent further challenges. Moreover, most of the resonant edges of interest occur at energies below 13 keV, where the absorption of the diamond anvils can be high enough to compromise the detection of the weak scattered signal (Sapelkin & Bayliss, 2001). Nonetheless, the newly found interest towards $5d$ transition metal compounds showing a large increase of the signal at energies where the diamonds are relatively transparent, together with further improvement of the synchrotron capabilities that allow a reduced beam size with high flux, reactivates the attention of the condensed matter community towards the HP-RXS experiments. For these reasons, the design of tailored HP instrumentation compatible with the demands of RXS is needed.

In this paper, we present a new HP-RXS setup to perform experiments in back-scattering configuration within 30–300 K and up to 20 GPa of pressure on I16, the Materials and Magnetism beamline at Diamond Light Source (Collins *et al.*, 2010). The new setup includes a membrane-driven DAC, an optical system to measure pressure *in situ* and a custom-designed panoramic dome. Some of the preliminary tests performed are also shown, proving the feasibility of this experimental approach.

2. HP setup for RXS

In order to design a high-pressure setup for RXS we need to overcome the following technical challenges.

We need a pressure cell with a large opening in order to maximize the scattering angle and, therefore, with access to reciprocal space while maintaining its mechanical strength.

It must be compact enough to operate at low temperature for two reasons: the limited space inside cryogenic devices and the fact that the smaller the mass inside the cryostat the easier it is to reach thermal equilibrium. Ideally, it should be machined from material that has high thermal conductivity and low thermal expansion, while remaining mechanically strong at low temperature. The design must also provide the means of changing and measuring pressure *in situ* in the whole range of temperature. Finally, it is necessary to reach a compromise between the dimensions of diamond anvils and sample. The smaller the culets of the anvils, the higher the pressure we can access, but the smaller the size of the crystal that we can fit in the sample chamber and therefore the scattered signal we obtain. Additionally, the detection of the scattered peaks also depends on the contribution of the diamond scattering into the background noise and the absorption of radiation by the diamond anvils, which changes significantly with the incident X-ray energy and becomes particularly critical below 7 keV (Sapelkin & Bayliss, 2001).
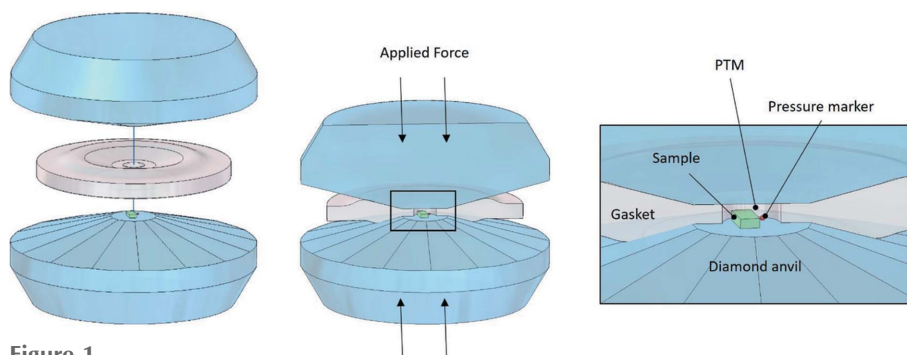

Figure 1
Illustration of the assembly and the main components of a diamond anvil cell: opposed diamond anvils, metallic gasket and sample space. The image on the right also shows in detail the elements placed in the sample chamber: sample, PTM and pressure marker.
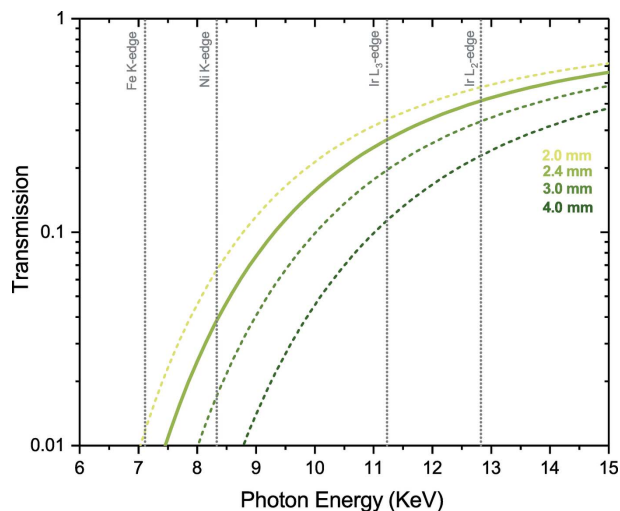
Figure 2
X-ray transmission (note the logarithmic scale) through diamond anvils of thickness between 1.0 and 2.0 mm for the range of energy between 6 and 15 keV calculated from Henke *et al.* (1993). We consider that the total thickness that the X-rays need to cross is twice the thickness of one anvil. For the anvils employed in our experiments, 1.2 mm thick, the X-rays need to go through a total thickness of 2.4 mm of anvil material (solid line). The dotted vertical lines represent some of the most common resonant edges of interest.

In Fig. 2, we can see how the thickness of the anvils plays a key role in the feasibility of the HP-RXS experiments. Small changes in the thickness result in significant variations in the transmitted signal. The anvils employed in our cell are a thinner version of the commercially available Boheler–Almax cut (Boehler & Hantsetters, 2004), with a final thickness of 1.2 mm. If we consider the total path of the incident and outgoing photons, the X-rays travel through a minimum thickness of 2.4 mm when perpendicular to the diamond face. Under these conditions, the minimum energy accessible without a huge reduction of the incident beam is just above 7.5 keV (solid line in Fig. 2). Other authors found a good solution using wide-angle partially drilled anvils in Laue geometry (Feng *et al.*, 2014; Wang *et al.*, 2016). In this case, a conical partial perforation of 60° reduces the total thickness of diamond crossed by the X-ray beam under 1 mm. However, for the back-scattering configuration chosen for the present design, such a solid angle limits considerably the access to the reciprocal space.

In the following sections, we describe the different parts of the experimental setup for HP-RXS experiments, including a detailed description of its operation.

2.1. Cell design

The proposed system was designed for use with the instrumentation available on I16, in particular a 4 K closed-cycle cryostat (D-202N) mounted on a Newport six-circle kappa goniometer. Keeping in mind the limited space available to host the cell, we designed a membrane-driven DAC inspired by the Merrill–Basset idea (Merrill & Bassett, 1974) with three pins for alignment and three screws as the locking mechanism. In Fig. 3, we can see a cross-sectional and a exploded view of the CAD model of the cell.

The material chosen for constructing the upper and lower body (parts 10 and 3 in Fig. 3), the piston (6) and the cryostat holder (2) is a CuBe alloy, BERYLCO25 from NGK (NGK-alloys, 2019), which combines non-magnetic behaviour with good thermal conductivity and mechanical high strength at low temperature (LT).

The cell presents an asymmetric design, with a panoramic aperture of 100° in the top part and a bottom half dedicated to the regulation and measurement of pressure. Unlike the original Merrill–Basset design, where the force is generated by tightening the locking screws (11 in Fig. 3), our design includes a gas membrane (4) that pushes the piston (6) and transmits the force towards the sample cavity. The gas membrane is hosted within the bottom half of the cell body avoiding the use of any additional fastening mechanism that would increase the overall thickness of the cell. When assembled, the cell is approximately 20–21 mm high, and fits into a circle of external diameter of 57 mm (circumference tangential to the triangular profile). This latter requirement is largely imposed by the required area of the gas membrane in order to reach the target
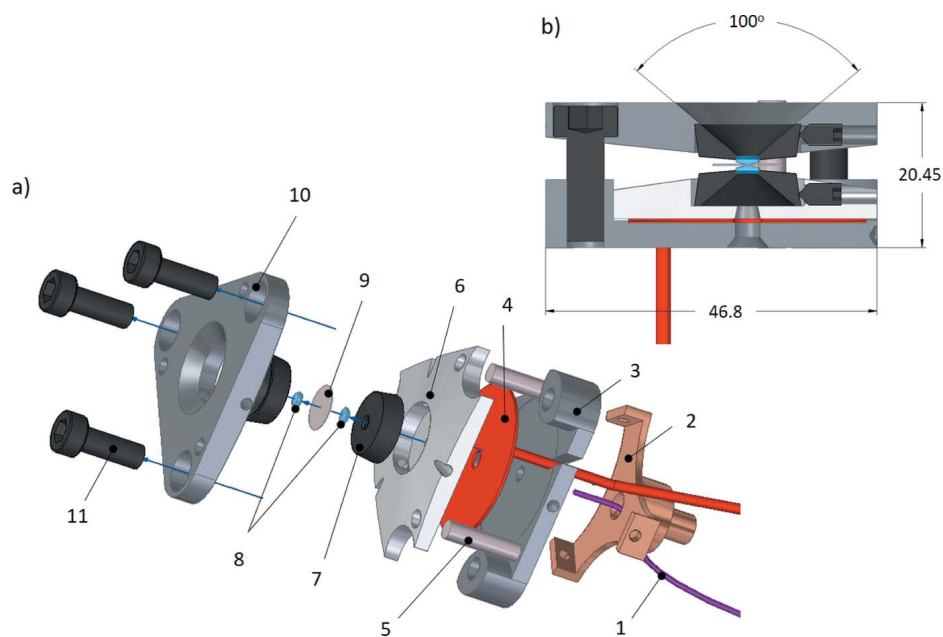

Figure 3
(*a*) Exploded view of the CAD model of the pressure cell. (1) Fibre optic, (2) cryostat adapter, (3) lower-body, (4) gas membrane, (5) alignment pin, (6) piston, (7) tungsten carbide seats, (8) diamond anvils, (9) gasket, (10) upper body and (11) M5 locking screws. (*b*) Section view of the cell with key dimensions in mm (opening angle in degrees).

pressure in the sample chamber. Taking into account the definition of pressure, $P = F/A$, we considered the target average pressure of 16 GPa at the anvil level, 120 bar in the membrane (36% under the safe limit of the gas controller, 190 bar) and oversized culets of 900 µm (12% larger than the maximum culet size considered for real experimental conditions) in order to compensate for the loss of force due to the friction between the various moving parts of the cell. Although the mechanism of pneumatic actuation was first proposed by Letoullec *et al.* (1988), our membrane design is more similar to the style of double-sided diaphragms (Daniels & Ryschkewitsch, 1983; Sinogeikin *et al.*, 2015). Our membranes are much more compact as they are built by welding two circular pieces of stainless steel foil, each 0.2 µm thick, with a final external diameter of 33.5 mm (35% smaller than the American counterparts) and with an inner hole of 4 mm. After use, the total thickness of the membrane changes to 0.5–0.7 mm. Attached to one of the faces is a metallic capillary (1 mm outer diameter) to introduce the gas and generate the force. For assessing the safe pressure limit of the membrane, a controlled burst test found a failure pressure of 850 bar, more than 600 bar over the maximum intended working pressure employed during our experiments.

We considered two options for the geometry of the experiment with the scattering plane crossing the diamond anvils. In Fig. 4(*a*) we show the Bragg geometry (back-scattering), where the reflected X-rays are collected though the same side of the cell through which the incident beam hits the sample; and in Fig. 4(*b*) the Laue configuration (transmission), where the scattered light is collected from the side opposite to the exciting beam. In Bragg geometry, we can use thicker samples, which are easier to prepare, and which also provide access to the high-angle region of the reciprocal space richer in reflections. In Laue geometry, the alignment of the sample in the beam is easier to conduct; the drop in the intensity of the transmitted signal due to the presence of the sample is larger than in the back-scattering geometry. This is the approach followed by Feng *et al.* (2014), using partially perforated diamonds to reduce the diamond absorption in transmission geometry. However, moving back to the comparison between Bragg and Laue configurations, in our particular case, to reach the same target pressure in transmission we would need a larger cell body in order to accommodate a larger membrane. Thus to obtain a symmetric scattering angle in both sides of the cell while keeping the same area in the membrane, its external diameter would be significantly larger. Under these conditions, the sample chamber would be easily above the centre of rotation without possibility of adjustment. For this reason, we found the back-scattering configuration as the most convenient for coupling with our current instrumentation arrangement.

Alternative designs with the scattering plane across the metallic gasket to avoid the absorption of radiation of the diamond anvils have been proposed by other authors (Kernavanois *et al.*, 2005). In these cells, a wider scattering angle can be accessed as well as absorption edges of lower energy. Despite these advantages, they employ beryllium as the gasket material, which is widely known for its toxicity and requires special dedicated handling instrumentation which is not currently compatible with the regulations at Diamond.

The back-scattering configuration leaves free the bottom face of the cell that can be employed for hosting the optics needed for the pressure measurement using the ruby fluorescence method (Piermarini *et al.*, 1975). To this end, we developed an optical system that consists of two sections: a bifurcated fibre in the external part of the cryostat, made of six individual laboratory-grade cores, 300 µm in diameter and 2.5 m long, assembled in two legs (5 + 1) from Ocean Optics; and a single core fibre (1 mm thick) inside the cryogenic device. The three ends of the bifurcated fibre are connected through SMA connectors to a 532 nm diode laser, a portable spectrometer from Ocean Optics (MayaPro4000) and the single core fibre inside the cryostat. The end of the inner fibre in the proximity of the sample chamber is a manually polished free end with no fitting.

A number of alternative models for the optical setup were tested including additional mirrors and collimation lenses. However, the loss of light due to the transfer between different optical elements was found to be larger than in the system adapted for our cell and described above.

2.2. Panoramic dome

In addition to the pressure cell, a panoramic dome has been designed specifically for the HP-RXS experiments. The dome is machined from steel 304L; it presents a cylindrical structure divided into three sections with a total height of 27.3 cm over the base of the cryostat and 10.2 cm in diameter. The possibility of assembling the dome in three separate parts allows its top section to be easily replaced to accommodate different experimental geome-
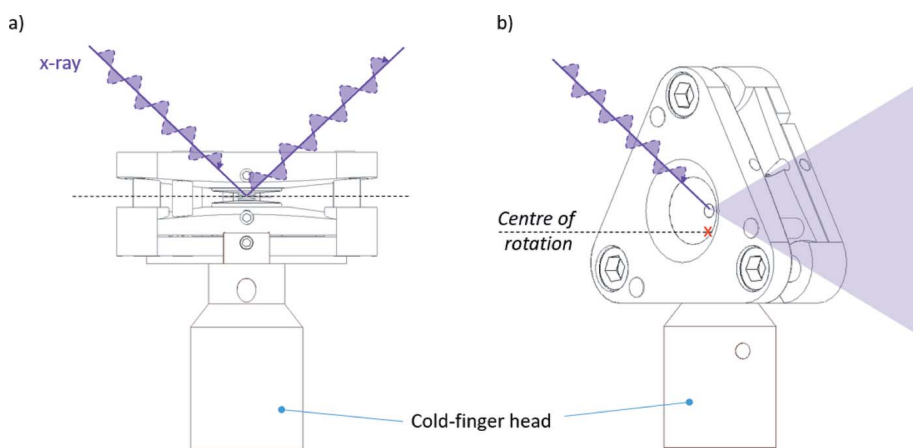

a)

x-ray

b)

Centre of rotation

Cold-finger head

Figure 4
View of the back-scattering (*a*) and transmission (*b*) configurations.

Figure 5
CAD-model of (*a*) the cryostat dome with details of the feed-throughs dedicated to the gas capillary and the fibre optics and the different optical windows. (*b*) Section view with details of the interior of the cryostat in the proximity of the pressure cell. Shaded areas represent the scattering angle at the top and lateral optical access at the bottom.

tries. In Fig. 5, we show a CAD model with some of the main features of the design.

In this first version of the dome, the upper section is specifically designed for experiments in back-scattering with three kapton windows: a panoramic aperture at the top for the scattering of the X-rays and two lateral windows for optical access. Kapton and beryllium are the only reliable materials employed for windows in cryogenic devices due to their low absorption of X-rays. Kapton allows visual examination of the cell while showing a reasonable durability to conduct the experiments and offers a reasonable transmission above 7 keV. The lower section of the dome presents four fitting ports, one of them dedicated to the insertion of the gas capillary for pressure regulation and the second one for the fibre optics. In order to prevent large oscillations of temperature when pumping gas into the membrane, the gas capillary is attached to the first stage of the cryostat so the gas is pre-cooled before reaching the cell body. In Fig. 6, we provide a photograph of the real pressure cell and the setup for HP-RXS experiments.

2.3. Loading and operation

In order to perform an HP-RXS experiment, we start by loading the pressure cell. First, the sample is placed as described before between the two tips of the diamond anvils, centred in the hole of a pre-indented metallic gasket (see Fig. 1). Once the sample is in the desired orientation, we include the pressure marker and the PTM in the sample chamber. Then, the cell is clamped by tightening the three M5 screws and mounted on the head of the cold finger. Once the cell is mounted on the cryostat, the next step is the alignment of the sample in the centre of rotation of the diffractometer. In a first approximation, with the cryostat open as in Fig. 6(*a*), we adjust the sample position optically by using a set of cameras in different orientations. Then, using the X-ray beam, we scan the gasket hole along the three directions of the space *x*, *y* and *z*, looking for a drop in the diffuse scattering from the diamond due to the presence of the sample. In order to look for a drop along the *z* axis [see system of coordinates in Fig. 6(*b*)], assuming the sample is flat and parallel to the diamond tips, we rotate the cell $\pm 5^{\circ}$ around an axis normal to *z*. Then, with the sample tilted, we scan along the *z* axis and we update the sample position to the point where the absorption is at its maximum. Now we are in a position to start looking for diffraction peaks. After finding a couple of reflections with their corresponding *hkl* indices, we can build an orientation matrix to navigate in the reciprocal space and to reach the position of the reflections of interest.

Once the alignment of the sample at room temperature is complete, we can start cooling down the system. Due to the limited space inside the cryostat we need to operate without any sort of thermal shielding but the actual dome. This limits the minimum temperature reachable to 30.5 K, with an approximate cooling time of 2.5 h (see Fig. 7). The increased base temperature is due mainly to the mass of the cell and the absence of the thermal shield. A temperature difference is observed between the head of the cold finger and the cell body (Fig. 7, inset).
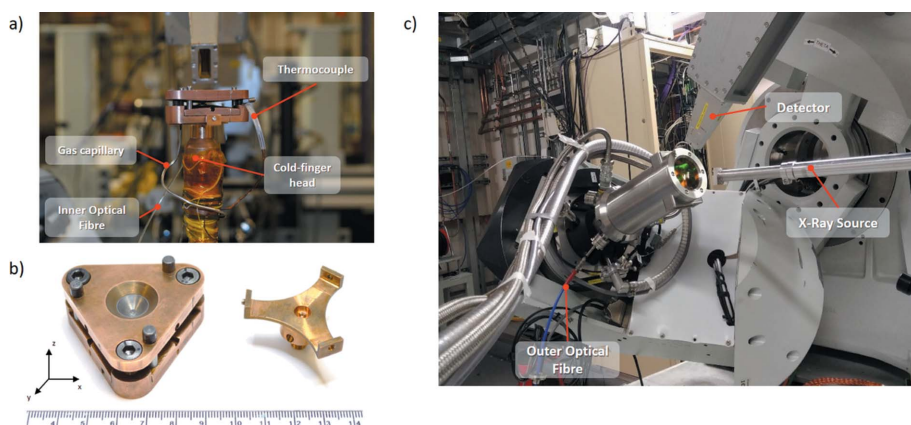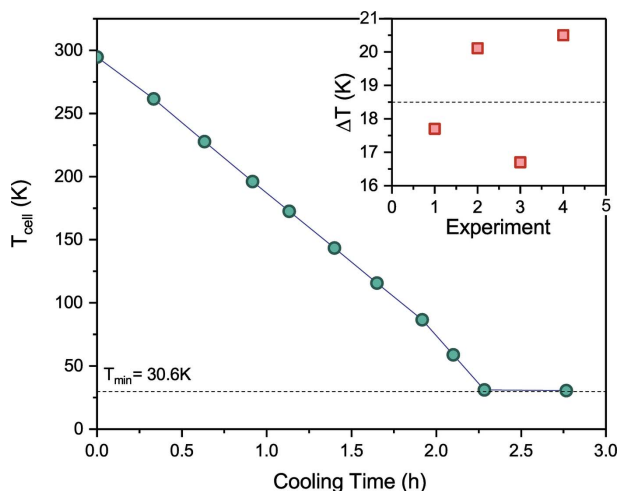
During the cooling process, the height of the sample changes due to the thermal contraction of the different parts of the cryostat. This height variation is reproducible, so it is possible to estimate the correction in sample height based on the measured sample temperature. In order to produce a reliable temperature variation, the cryostat is held at base temperature while the sample temperature is

Figure 6
Pictures of the setup for HP-RXS experiments. (*a*) Pressure cell mounted on the cold finger. Detail of the thermo-couple, optical fibre, gas capillary and cold-finger head. (*b*) Pressure cell and cryostat coupling piece. (*c*) HP-RXS setup on I16. Detail of the X-ray source, optical fibre and detector.
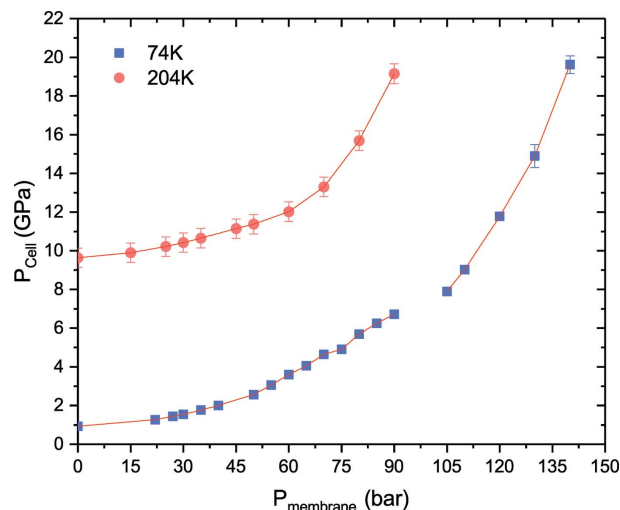
Figure 7
Cooling time of the cell mounted inside the cryostat from ambient to base temperature. The dashed line shows the minimum temperature reached. The inset shows the temperature difference, ΔT (K), between the top of the cold finger and the cell body for different experiments. The dashed line in the inset shows the average value of the temperature difference.

Figure 8
Results of the pressure test performed at 74 K and 204 K with blue squares and red dots, respectively. Pressure in the cell in GPa as a function of the pressure in the membrane in bars. The first determined using the ruby fluorescence technique, the second regulated using a GE Druck PACE5000 gas controller. The cell was prepared using 4:1 methanol:ethanol as PTM and it was closed initially at 1 GPa. The test was performed in the first place at 74 K reaching a maximum pressure close to 20 GPa. Then the pressure in the membrane was released and the test was repeated at 204 K.

controlled using a heater. Therefore, even for the cases when a particularly low temperature is not required, initially the system needs to be cooled down to base temperature. When the target temperature in the cell is reached, we can look for the reflections resulting from the electronic correlation of interest, realign the sample position using the signal of the peak under study (x, y, z scans described above maximizing the peak intensity) and start the RXS experiment.

Pressure is controlled by pumping helium gas into the membrane that pushes up the piston increasing the force in the sample chamber. In Fig. 8, we can see the evolution of the level of pressure in the cell against the pressure in the membrane for two different temperatures. The two pressure tests were performed using anvils with culets of 500 μm, 4:1 methanol:ethanol (ME) as PTM and a steel gasket (initially 200 μm thick) pre-indented down to 107 μm thickness. The cell was loaded with a piece of ruby at an initial pressure of 1 GPa and mounted on the cryostat. Then, the temperature was stabilized, firstly at 74 K and the pressure was increased, reaching a maximum value close to 20 GPa measured by the ruby fluorescence method and corrected to the actual temperature. After that, the pressure in the membrane was released and the test was repeated at 204 K. In both cases, we found a deterioration of the ruby signal (broadening of the peaks and loss of intensity) at the same critical pressure that can be attributed to the lost of hydrostaticity at these conditions and to the fact that the sample chamber is further away from the fibre optics tip as we keep on increasing pressure by inflating the membrane.

Additionally to the pressure experiment, extra tests were performed in order to further develop the correct experimental methodology, determining the time required to stabilize the system when carrying out small variations of temperature and to explore the possibility of using gold as an alternative for pressure determination. In order to do so, we

prepared the membrane cell using anvils with culets of 800 μm, a steel gasket indented down to 116 μm and drilled with a 500 μm hole in the centre of the indentation. Then, the cell was loaded with gold and ruby using 4:1 ME as PTM. Several pressure–temperature (P–T) points were reached observing that for temperature increments of 5–10 K a stabilization time of 35–40 min is required in order to reach the thermal equilibrium. This long stabilization time is an expected consequence of the temperature difference observed between the head of the cold finger and the cell body (see Fig. 7, inset), that could be improved using better insulation from the exterior, improving further the thermal contact between the cell and the cold finger and miniaturizing the cell.

For several of the experimental P–T points reached, we measured the level of pressure using the dependence of the ruby fluorescence shift applying the temperature correction from Datchi *et al.* (2007) and the equation of state of gold from Holzapfel *et al.* (2001). The results obtained can be seen in Fig. 9. For the gold scale, the values of pressure were obtained by averaging the lattice parameters calculated from the position of the reflections (511), (531) and (442) and applying the equation of state mentioned.

Both methods provide reasonably similar values of pressure up to 4 GPa, from where we observed an underestimation from ruby with respect to the gold gauge. This discrepancy between the two approaches might be the result of a combination of deviatoric stress arising from the solidification of the pressure medium (non-hydrostaticity) (Torikachvili *et al.*, 2015) and the fact that the crystal of ruby and the piece of gold might not be exposed to the same stress due to the pressure gradient along the sample chamber (Mao, 1978).
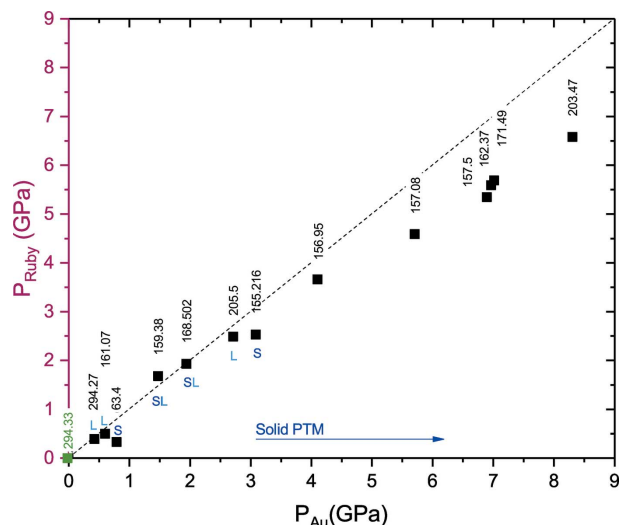
Figure 9
Comparative measurement of pressure for different experimental conditions using the pressure shift of the R1 luminescence line of ruby (Datchi *et al.*, 2007) and the equation of state of gold from Holzapfel *et al.* (2001). All the pressure points were acquired using the same loading for different temperature and pressure conditions. The temperature for each point is given (vertical) above the each data point. 'S' and 'L' stand for the state of the pressure media (4:1 methanol:ethanol), 'solid' or 'liquid', respectively. The first point in green corresponds to the reference for ruby and gold at room conditions.

In favour of experimental simplicity, the ruby gauge is more convenient. At the moment, the gas control unit for the membrane is placed inside the experimental hutch and cannot be controlled remotely from the control room. Therefore, pressure-tuning requires switching off the beam, entering the hutch and manually operating the gas membrane. Once we are inside the hutch, whereas the ruby method allows the level of pressure to be estimated directly in a few seconds, the use of gold requires exiting the hutch once again, interlocking, switching on the beam, aligning at the gold position and acquiring the diffraction pattern. In some cases, we may need to repeat this sequence of steps several times until reaching the aimed level of pressure, increasing significantly the time employed (from minutes to hours compared with the ruby method). A second aspect that makes the use of gold less suitable is the fact that the addition of extra components in the sample chamber represents an extra source of background noise that in some cases may be critical when trying to detect particularly weak resonant signals. For our particular experimental conditions and for the reasons just mentioned, we consider the ruby fluorescence a better approach to estimate pressure.

We also experienced some issues due to the chemical reactivity of the different substances present in the sample chamber when exposed to the X-ray radiation that hampered our progress in establishing the correct experimental method. On several occasions we observed photon-induced chemical reactions in the sample chamber that degraded the quality of the sample and prevented us from observing the signals of interest. We tried different loading combinations of PTM (4:1 ME, 1:1 *n*-pentene:isopentane, Silicone oil, Daphne oil

7373, NaCl, KCl) and substances employed to fix the sample position (Vaseline, vacuum grease and superglue), finding that not the loading combination but only the attenuation of the beam was effective in preventing the reactions from happening. At the energy range employed in our experiments (8–13 keV), the absorption cross-section of X-rays is larger than for higher energy, making the lighter elements in the transmitting media more prone to undergo chemical reactions. Helium gas loading was also considered to reduce the reactivity of the sample chamber components. However, a contraction in the chamber volume to 5–10% of the initial value at HP–LT is expected when using stainless steel gaskets (Feng *et al.*, 2010), which requires initial thin samples, 10 μm × 10 μm × 5 μm, that would not take full advantage of the full flux of the focused beam. A number of HP-RXS studies in the literature consider 4:1 ME as the best option for PTM (Feng *et al.*, 2010, 2014; Wang *et al.*, 2016, 2019). On the other hand, only 6 GPa of pressure at 200 K are sufficient to solidify He (Mao *et al.*, 1988; Loubeyre *et al.*, 1993). Thus, it is not clear that He provides a significant improvement in hydrostaticity over 4:1 ME at LT. The attenuation of the incident beam down to 2% of the full intensity seems to be enough to avoid the degradation of 4:1 ME loadings and was adopted as the preferred methodology. Besides the attenuation of the beam, the use of steel as the gasket material was also found to be the most adequate for our experiments. The emission lines of Fe, $K_{\alpha 2}$ (6.390 keV) and $K_{\beta 1}$ (7.057 keV), are far enough from the range of energy employed in our experiments in order to discriminate completely from the signal using the detector energy threshold. Other gasket materials such as Re, commonly used for the higher-pressure range, were found not suitable for this reason.

3. Experimental application

An HP-RXS study on the magnetic order of $Sr_3Ir_2O_7$ was conducted on I16 using the developed instrumentation. $Sr_3Ir_2O_7$ is an intermediate case ($n = 2$) of the Ruddlesden–Popper (RP) series of layered iridates $Sr_{n+1}Ir_nO_{3n+1}$ that presents tetragonal structure at ambient conditions ($I4/mmm$, $a = 3.9026$ Å, $c = 20.9300$ Å) (Subramanian *et al.*, 1994) and magnetic order at relatively high temperature ($T_N = 285$ K) (Boseggia *et al.*, 2012). In this family of compounds the interplay between the octahedral crystal field and the strong spin–orbit coupling at the Ir^{4+} ($5d^5$) sites combined with the layered structure give rise to a rich landscape of fascinating properties (Moon *et al.*, 2008).

In particular, $Sr_3Ir_2O_7$ is specially suitable for the HP-RXS study for several reasons. Firstly, the Ir L_3 absorption edge (11.215 keV) falls within the energy range where the diamond anvil absorption is not so strong to compromise the observation of magnetic reflections, as it is the case for other elements, *i.e.* rare-earths. Secondly, this kind of perovskite structures presents a natural tendency of the transition metal oxygen octahedra to rotate and distort under a small compression, that may affect the strength and sign of the magnetic exchange interactions. Finally, the relatively high ordering temperature

makes easier the experimental conditions for this first experiment.

The full results of this study are beyond the scope of this paper and are to be published in a separate document. Hence, in Fig. 10 (left) we show the magnetic reflection (0.5, 0.5, 34) and the Bragg peak (1, 1, 34) collected at 2.4 GPa and 150 K using the experimental setup described here. In Fig. 10 (right) we can see a comparison between the energy scan collected under the same experimental conditions at the magnetic reflection (0.5, 0.5, 34) and the fluorescence of the sample acquired in transmission geometry at 2.2 GPa and 200 K using a different system (Jin *et al.*, 2017). The measured intensity of the magnetic reflections in this system is about one-tenth of that of an average charge reflection. This same ratio applies for the loss of intensity observed when introducing the samples in the pressure cell with respect to the bare crystal. The collection time for these measurements was usually 1 s per point, obtaining a typical signal-to-noise ratio of 2:1 for the magnetic signals.

In summary, we have developed a high-pressure system for HP-RXS experiments on I16. It includes an asymmetric membrane-driven diamond anvil cell for operation in back-scattering geometry, with a solid opening angle of 100°. The system is fitted with a set of fibre optics that connects the external and internal part of the cryostat, allowing the measurement of pressure *in situ* using the luminescence of ruby. This setup has been tested for pressures up to 20 GPa and temperatures down to 30.6 K. A study on the magnetic order of $Sr_3Ir_2O_7$ was conducted and some of the experimental data obtained are shown, proving the viability of the proposed methodology. The compactness of the cell allows to potentially couple it to other cryostat models available at most large facilities. Simple modifications of the cell body and the dome could be easily done to accommodate it for use at other beamlines. Although a size reduction of the cell body is not possible without weakening the membrane capacity, exploring alternatives to reduce the dimensions of the pressure cell that would allow operation in transmission geometry and reaching lower values of minimum temperature would be convenient. We also consider that the addition of a more complex external setup for the measurement of the ruby fluorescence would improve the system's reliability and ease of use. It is not clear whether or not the increase in hydrostaticity of helium over 4:1 methanol:ethanol as the PTM is significant in the low-temperature regime. However, further insight into this question would also be of interest to the future developments.

Figure 10
(*a*) Measurement of the magnetic and Bragg reflections (0.5, 0.5, 34) (green dots) and (1, 1, 34) (blue squares) of $Sr_3Ir_2O_7$ collected at 2.4 GPa and 150 K. (*b*) Energy scan on the magnetic peak (0.5, 0.5, 34) (half-filled green dots) collected under the same conditions. The solid black line shows the fluorescence collected from a different sample of the same batch at 2.2 GPa and 200 K in transmission, using an alternative setup more limited in temperature.

References

Agrestini, S., Mazzoli, C., Bombardi, A. & Lees, M. R. (2008). *Phys. Rev. B*, **77**, 140403.

Biffin, A., Johnson, R. D., Kimchi, I., Morris, R., Bombardi, A., Analytis, J. G., Vishwanath, A. & Coldea, R. (2014). *Phys. Rev. Lett.* **113**, 197201.

Blume, M. & Gibbs, D. (1988). *Phys. Rev. B*, **37**, 1779–1789.

Boehler, R. & De Hantsetters, K. (2004). *High. Press. Res.* **24**, 391–396.

Boseggia, S., Springell, R., Walker, H. C., Boothroyd, A. T., Prabhakaran, D., Wermeille, D., Bouchenoire, L., Collins, S. P. & McMorrow, D. F. (2012). *Phys. Rev. B*, **85**, 184432.

Calder, S., Garlea, V. O., McMorrow, D. F., Lumsden, M. D., Stone, M. B., Lang, J. C., Kim, J.-W., Schlueter, J. A., Shi, Y. G., Yamaura, K., Sun, Y. S., Tsujimoto, Y. & Christianson, A. D. (2012). *Phys. Rev. Lett.* **108**, 257209.

Collins, S. P., Bombardi, A., Marshall, A. R., Williams, J. H., Barlow, G., Day, A. G., Pearson, M. R., Woolliscroft, R. J., Walton, R. D., Beutier, G., Nisbet, G., Garrett, R., Gentle, I., Nugent, K. & Wilkins, S. (2010). *AIP Conf. Proc.* **1234**, 303–306.

Daniels, W. B. & Ryschkewitsch, M. G. (1983). *Rev. Sci. Instrum.* **54**, 115–116.

Datchi, F., Dewaele, A., Loubeyre, P., Letoullec, R., Le Godec, Y. & Canny, B. (2007). *High. Press. Res.* **27**, 447–463.

Drozdov, A. P., Kong, P. P., Minkov, V. S., Besedin, S. P., Kuzovnikov, M. A., Mozaffari, S., Balicas, L., Balakirev, F. F., Graf, D. E., Prakapenka, V. B., Greenberg, E., Knyazev, D. A., Tkacz, M. & Eremets, M. I. (2019). *Nature*, **569**, 528–531.
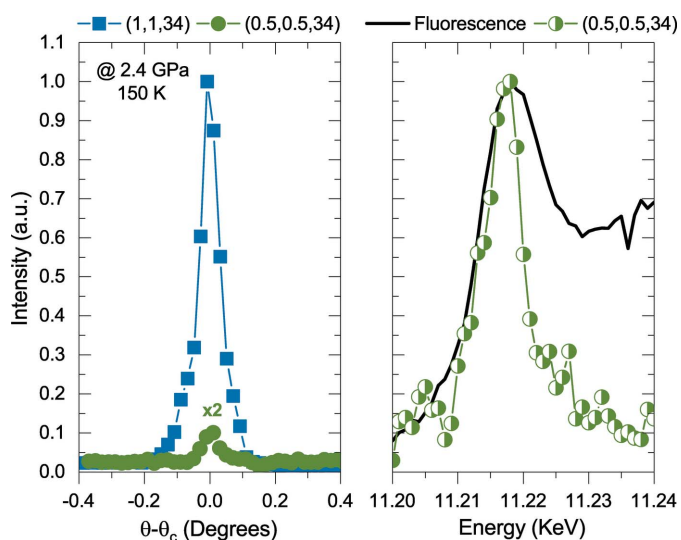
Fabrizi, F., Walker, H. C., Paolasini, L., de Bergevin, F., Fennell, T., Rogado, N., Cava, R. J., Wolf, T., Kenzelmann, M. & McMorrow, D. F. (2010). *Phys. Rev. B*, **82**, 024434.

Feng, Y., Jaramillo, R., Wang, J., Ren, Y. & Rosenbaum, T. F. (2010). *Rev. Sci. Instrum.* **81**, 041301.

Feng, Y., Wang, J., Palmer, A., Aguiar, J. A., Mihaila, B., Yan, J.-Q., Littlewood, P. B. & Rosenbaum, T. F. (2014). *Nat. Commun.* **5**, 4218.

Gibbs, D., Harshman, D. R., Isaacs, E. D., McWhan, D. B., Mills, D. & Vettier, C. (1988). *Phys. Rev. Lett.* **61**, 1241–1244.

Henke, B., Gullikson, E. & Davis, J. (1993). *At. Data Nucl. Data Tables*, **54**, 181–342.

Hill, J. P. & McMorrow, D. F. (1996). *Acta Cryst.* A**52**, 236–244.

Holzapfel, W. B., Hartwig, M. & Sievers, W. (2001). *J. Phys. Chem. Ref. Data*, **30**, 515–529.

Jin, H., Woodall, C. H., Wang, X., Parsons, S. & Kamenev, K. V. (2017). *Rev. Sci. Instrum.* **88**, 035103.

Kernavanois, N., Deen, P. P., Paolasini, L. & Braithwaite, D. (2005). *Rev. Sci. Instrum.* **76**, 083909.

Lee, N., Vecchini, C., Choi, Y. J., Chapon, L. C., Bombardi, A., Radaelli, P. G. & Cheong, S.-W. (2013). *Phys. Rev. Lett.* **110**, 137203.

Letoullec, R., Pinceaux, J. P. & Loubeyre, P. (1988). *High. Press. Res.* **1**, 77–90.

Loubeyre, P., LeToullec, R., Pinceaux, J. P., Mao, H. K., Hu, J. & Hemley, R. J. (1993). *Phys. Rev. Lett.* **71**, 2272–2275.

Mao, H. K. (1978). *Science*, **200**, 1145–1147.

Mao, H. K., Hemley, R. J., Wu, Y., Jephcoat, A. P., Finger, L. W., Zha, C. S. & Bassett, W. A. (1988). *Phys. Rev. Lett.* **60**, 2649–2652.

Merrill, L. & Bassett, W. A. (1974). *Rev. Sci. Instrum.* **45**, 290–294.

Moon, S. J., Jin, H., Kim, K. W., Choi, W. S., Lee, Y. S., Yu, J., Cao, G., Sumi, A., Funakubo, H., Bernhard, C. & Noh, T. W. (2008). *Phys. Rev. Lett.* **101**, 226402.

Nakamura, F. (2007). *J. Phys. Soc. Jpn*, **76**, A96–A99.

NGK-alloys (2019). *NGK*, http://www.ngk-alloys.com.

Pascut, G. L., Coldea, R., Radaelli, P. G., Bombardi, A., Beutier, G., Mazin, I. I., Johannes, M. D. & Jansen, M. (2011). *Phys. Rev. Lett.* **106**, 157206.

Piermarini, G. J., Block, S., Barnett, J. D. & Forman, R. A. (1975). *J. Appl. Phys.* **46**, 2774–2780.

Poudel, N., Gooch, M., Lorenz, B., Chu, C. W., Kim, J. W. & Cheong, S. W. (2015). *Phys. Rev. B*, **92**, 144430.

Sapelkin, A. V. & Bayliss, S. C. (2001). *High. Press. Res.* **21**, 315–329.

Sinogeikin, S. V., Smith, J. S., Rod, E., Lin, C., Kenney-Benson, C. & Shen, G. (2015). *Rev. Sci. Instrum.* **86**, 072209.

Subramanian, M., Crawford, M. & Harlow, R. (1994). *Mater. Res. Bull.* **29**, 645–650.

Torikachvili, M. S., Kim, S. K., Colombier, E., Bud'ko, S. L. & Canfield, P. C. (2015). *Rev. Sci. Instrum.* **86**, 123904.

Wang, Y., Feng, Y., Cheng, J.-G., Wu, W., Luo, J. L. & Rosenbaum, T. F. (2016). *Nat. Commun.* **7**, 13037.

Wang, Y., Rosenbaum, T. F. & Feng, Y. (2019). *IUCrJ*, **6**, 507–520.

Waterfield Price, N., Johnson, R. D., Saenrang, W., Maccherozzi, F., Dhesi, S. S., Bombardi, A., Chmiel, F. P., Eom, C.-B. & Radaelli, P. G. (2016). *Phys. Rev. Lett.* **117**, 177601.